Journal of Volcanology and Geothermal Research 400 (2020) 106913

Contents lists available at ScienceDirect

Journal of Volcanology and Geothermal Research

journal homepage: www.elsevier.com/locate/jvolgeores

Visualizing preferential magmatic and geothermal fluid pathways via electric conductivity at Villarrica Volcano, S-Chile

Maximiliano Pavez [a,c,*], Eva Schill [a,b], Sebastian Held [c], Daniel Díaz [d], Thomas Kohl [c]

[a] Institute of Nuclear Waste Disposal, Karlsruhe Institute of Technology, Hermann-von-Helmholtz-Platz 1, 76344 Eggenstein-Leopoldshafen, Germany
[b] Institute of Applied Geosciences, Technical University Darmstadt, Schnittspahnstraße 9, 64287 Darmstadt, Germany
[c] Institute of Applied Geosciences, Karlsruhe Institute of Technology, Adenauerring 20B, 76131 Karlsruhe, Germany
[d] Departamento de Geofísica, Facultad de Ciencias Físicas y Matemáticas, Universidad de Chile, Blanco Encalada 2002, Santiago, Chile

ARTICLE INFO

Article history:
Received 11 September 2019
Received in revised form 5 May 2020
Accepted 6 May 2020
Available online 14 May 2020

Keywords:
Magnetotellurics
Fault zones
Structural control of fluid pathways
Villarrica Volcano

ABSTRACT

Preferential fluid pathways along regional fault systems are crucial for the spatial localization of volcanic and geothermal manifestations. Differences in electric properties of fluids and hydrothermal alteration products against the unaltered matrix allow for visualization of such pathways. Unfavorable geometry for 2-D inversion resulting from the fluid pathways in regional faults often being aligned along the geo-electric strike can be overcome by using 3D inversion of magnetotelluric data. For a section in the 1400 km long Liquiñe-Ofqui Fault System (LOFS), we demonstrate the potential of 3-D inversion of magnetotelluric data for visualization of fluid pathways. Six out of eight electric resistivity anomalies at intermediate depth are connected to volcanic or geothermal surface manifestations. Deep and highly conductive anomalies are detected in the vicinity of the volcanic chain and where the LOFS is crosscut by a fault that belongs to the Andean transversal fault system. The anomaly related to the fault crossing reveals a vertical pathway extending to the surface. Phase tensor analyses indicate a structural origin of the latter anomaly that may be connected to a line of volcanic cones that occurs in the NE of the Villarrica Volcano.

1. Introduction

Preferential fluid pathways in subduction settings at different scales result e.g. in volcanoes, monogenetic cones and thermal springs. They crosscut the crystalline basement which is typically characterized by low matrix porosity and permeability. Bulk porosity and permeability are mainly controlled by fracture network properties (Bense et al., 2013), which in turn depends on both the fracture network connectivity and the aperture distribution (Brown and Bruhn, 1998). Near fault zones, the fracture density and connectivity tend to increases significantly and thus, bulk rock permeability near fault zones is generally larger than that of the protolith (Bense et al., 2013). Shearing and brecciation, common in faults within brittle crystalline rocks such us basalts, can increase of permeability by as much as five orders of magnitude (Walker et al., 2013). The aperture of fractures is also very sensitive to the pressure and stress conditions in the rock, which lead to more permeable fracture networks under favorably-oriented stress (Barton et al., 1995). Thus, the heterogeneous distribution of a fault's core and damage zone in crystalline and volcanic rock leads to tortuosity and preferential flow paths (Bense et al., 2013).

Worldwide, zones of low resistivity within continental fault systems have been attributed to the presence of fluids of different type (Unsworth et al., 1999; Unsworth and Bedrosian, 2004a; Bredosian et al., 2004; Cordell et al., 2019). In volcanic environments, low resistivity has been interpreted as a sign if either hydrothermal fluids, conduits, magmatic deposits, or a combination of these features (Bertrand et al., 2012; Hill et al., 2009; Díaz et al., 2015). In geothermal systems, low resistivity is associated with hydrothermal alteration, revealing either a cap layer in volcanic environment (e.g. Heise et al., 2008) or changes to fracture networks in non-volcanic systems (Geiermann and Schill, 2010).

To visualize heterogeneities in the electric resistivity distribution along fault zones, one typically compares cross-sectional profiles across the fault zone by magnetotelluric technique (Jones and Groom, 1993; Unsworth and Bedrosian, 2004b). In contrast to earlier 2-D inversion of localized profiles, regional scale 3-D inversion of magnetotelluric data from the Lonquimay, Villarrica, and Llaima active volcanoes was able to reveal upper crustal conductors, interpretable as magma reservoirs (Kapinos et al., 2016).

The area extends from the Villarrica Volcano in the south to Pucón Lake in the north and runs along the Liquiñe-Ofqui Fault System

* Corresponding author at: Institute of Nuclear Waste Disposal, Karlsruhe Institute of Technology, Hermann-von-Helmholtz-Platz 1, 76344 Eggenstein-Leopoldshafen, Germany.
E-mail address: maximiliano.pavez@partner.kit.edu (M. Pavez).

https://doi.org/10.1016/j.jvolgeores.2020.106913
0377-0273/

(LOFS) intersected by the WNW-ESE aligned pre-Andean Mocha Villarrica Fault Zone (MVFZ), belonging of Andean Transfers Fault (ATF) (Perez-Flores et al., 2016). The fault zone is accompanied by the Villarrica-Quetrupillán-Lanín volcanic chain that trends N50°W (Lara, 2004). Along this LOFS section, one finds both geothermal springs (Sánchez et al., 2013; Wrage et al., 2017; Held et al., 2018) and monogenetic cones (Cembrano et al., 1996). Anomalously high electric conductivities found in the lower crust (Brasse and Soyer, 2001; Kapinos et al., 2016; Held et al., 2016) suggest a way to connect near-surface anomalies at the LOFS to their underlying roots.

Held et al., 2016 revealed substantial information about the geoelectric properties of the subsurface by means of two cross sections through the dominant geological structures. 2-D interpretation models based on the best geoelectric strike for all periods exhibits an NS trend (Brasse and Soyer, 2001; Held et al., 2016), validating the execution of 2-D inversion in transversal profiles of the strike to visualize the predominant structures on the strike. However, variation between shallow, intermediate and deep levels, ranging from a NS to N30–40°E and NS strike respectively, requires a three-dimensional inversion to study the effects of secondary geological structures, mainly to overcome problems with the 2-D inversion along the geoelectric strike.

The main objective of this study based on magnetotelluric data from Held et al. (2016) is clarify the 3-D effects generated by preferential fluid pathways in interaction areas between active cortical faults and volcanism surrounding the Villarrica area. In addition, provide a comparison of the results of electrical conductivity anomalies with the surface manifestations of the volcanic and geothermal system to conclude the potential origin of these anomalies.

2. Geological background

The volcanic and structural features of the study area are embedded in the compressive plate boundary system of the Southern Andes. Here, the subduction of the Nazca and Antarctic plates below the South American continental plate result in a system of parallel and oblique to the arc faults as well as a large number of active volcanoes. The study area is part of the Southern Volcanic Zone that includes regional faults, namely the Liquiñe-Ofqui Fault System (LOFS, López-Escobar et al., 1995) and a number of ATFs, which are associated with major volcanic eruption centers of Quaternary to recent age (Fig. 1a). In the northern part of LOFS, the regional stress field is characterized by a maximum sub-horizontal compressive regime trending in N60°E direction (Lavenu and Cembrano, 1999; Rosenau et al., 2006). Besides the volcanic systems, the study area is characterized by a large number of thermal springs (Fig. 1b). In the following, major structures and the thermal springs are detailed.

2.1. Liquiñe-Ofqui Fault System

Extending over >1200 km, this prominent fault system runs parallel to the N–S oriented volcanic chain of the Southern Andes and is associated with a dextral transpressional regime (Cembrano et al., 1996; Cembrano et al., 2000). In the north, it reaches the Lonquimay-Tolhuaca volcanic complex, where it has been described as a "horsetail" that branches towards the east (Rosenau et al., 2006). A similar structure with bending the LOFS towards west is found at its southern rim in Patagonia. In its northern half, the LOFS is divided into two branches,

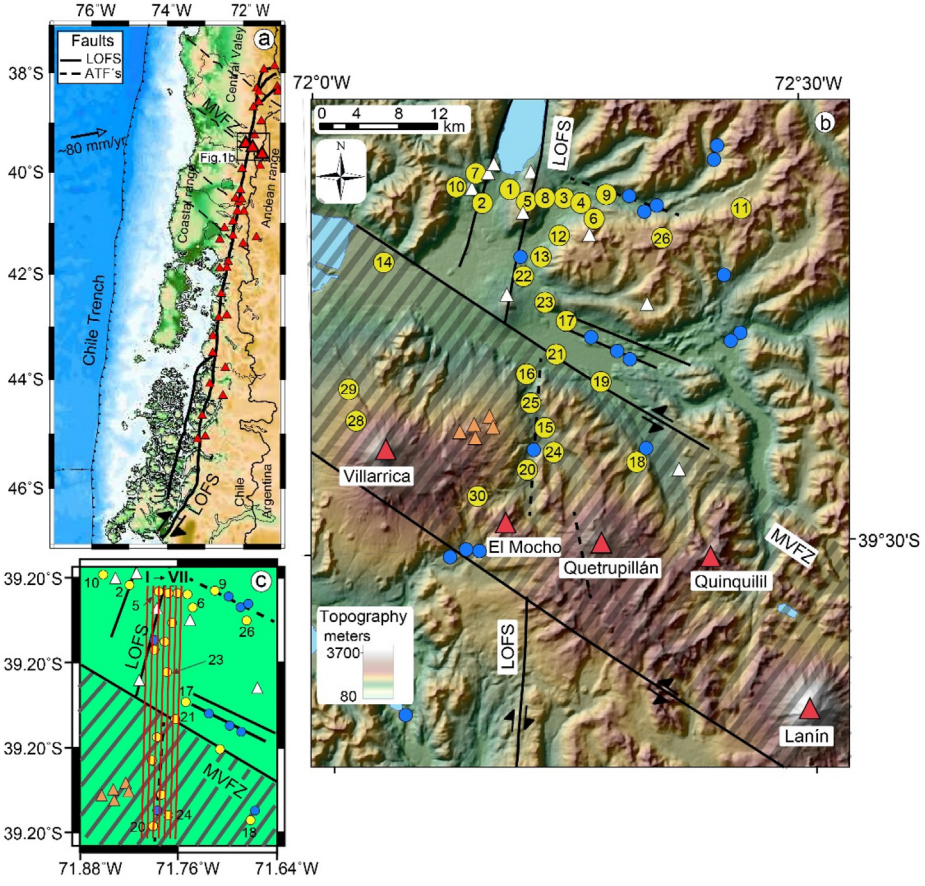

Fig. 1. a) Tectonic setting of the Southern Volcanic Zone including the Liquiñe Ofqui Fault System (LOFS), the Andean Transverse Faults (ATFs) and the main volcanic edifices (modified from Cembrano and Lara, 2009; Pérez-Flores et al., 2016; Somoza, 1998). b) Topographic map of the study area including the LOFS and further fault zones (black lines), the Mocha-Villarrica Fault Zone (MVFZ, dashed area), monogenetic cones (white triangles), Los Nevados group (orange triangles), major volcanic buildings (red triangles), and thermal springs (blue dots) (modified from Sánchez et al., 2013 and SERNAGEOMIN). Magnetotelluric sites are labeled with numbers in yellow dots. c) Seven N–S section across the LOFS.

of which the western on the dominant and structurally well-know. In this study, we neglect the eastern branch since it is at the rim of the study area. Moreover, the LOFS is offset during the reactivation of the ATFs.

Such an offset characterizes also the study area (Fig. 1b). Here, the LOFS north of the offset reveals two characteristic features. 1) It is split into two parallel branches running to east and west of Caburgua Lake. 2) Both branches are associated with groups of Holocene pyroclastic cones (Hickey-Vargas et al., 1989; Melnick et al., 2006) originating from different eruptive episodes and mostly of mafic composition (Lara et al., 2006a, 2006b). At the eastern branch, the monogenetic cones follow the local N10°E trend of the LOFS (Cembrano et al., 1996), whereas at the western branch a N50°E alignment is observed (Lara et al., 2006a). Both groups reveal similar geochemical compositions. Single monogenetic cones further to the east differ partly or significantly from this signature (Hickey-Vargas et al., 2016; McGee et al., 2017) and occur in an area of high density of thermal springs.

In the southern part of the study area, the LOFS is characterized by one single fault plane. The outline of LOFS through the ATF (corresponding to MVFZ in Fig. 1) is a matter of discussion. In their regional studies Lara and Moreno (2004), Rosenau et al. (2006) and Melnick et al. (2006) indicate an interruption and offset of LOFS throughout this fault zone. Yet in a more detailed study, Sánchez et al. (2013) and SERNAGEOMIN do not find clear evidence for the offset of the fault zone and just describe it as an inferred fault in the area to the north of the volcanic chain between Villarrica and Quetrupillán following the southern outline of LOFS.

2.2. Andean transverse faults

Kinematic condition along the LOFS result in NE and NW striking faults and volcanic alignments such as stratovolcanoes and monogenetic cones (Cembrano and Lara, 2009; Melnick et al., 2006; Cembrano et al., 2002). The oblique-to-the-arc ATFs develop in NNW-WNW directions. The major ATFs, namely Bío-Bío Aluminé, Lanalhue, MVFZ, and Valdivia fault zones (Fig. 1a), are oriented in parallel to the minimum horizontal stress and undergo active compression (Lara et al., 2006a; Cembrano and Lara, 2009). In this kinematic regime, the stratovolcanoes along ATFs reveal an elaborated magmatic evolution and eruptive styles due to the long residence of magma in the upper crust (Lara et al., 2004). In contrast, NE–SW oriented fractures facilitate a rapid rise of magma (Lara et al., 2006a; Cembrano and Lara, 2009). In the study area, such fault zones occur on the northeastern flank of the Villarrica Volcano (Cembrano and Lara, 2009).

At the Villarrica Volcano, the ATF is represented by the MVFZ that crosses the crystalline basement and displaces the LOFS by a few kilometers indicating a sinistral movement (Lange et al., 2008). The MVFZ accompanies the N50°W alignment of the Middle Pleistocene to Holocene Villarrica-Cordillera El Mocho-Quetrupillán-Quinquilil-Lanín volcanic chain (Lara et al., 2004). Of these, the Villarrica, Quetrupillán and Lanín volcanoes have erupted during Holocene times. The Villarrica Volcano, with a basaltic to andesitic-basaltic composition, builds on the MVFZ (Moreno and Clavero, 2006). This compressive tectonic situation, along with the overload exerted by the building of the Villarrica Volcano, is expected to hinder the rise of magma (Pinel and Jaupart, 2000) and thus, facilitating the accumulation of magma in shallow reservoirs (Hickey-Vargas et al., 1989). Both the volcanoes of the Villarrica-Quetrupillán-Lanín volcanic chain and the monogenetic cones root deep down to the mantle-crust boundary. In contrast to the Villarrica Volcano, the monogenetic cones do not have a shallow magma chambers, probably due to the role of the LOFS as an efficient conduit for the rise of magma (Hickey-Vargas et al., 1989; Morgado et al., 2015).

Cembrano and Lara (2009) proposed volcanic-tectonics associations based on spatial distribution and overall morphology of individual volcanoes and groups of volcanoes. Primarily controlled by the present-day compressional or dextral–transpressional tectonics of the volcanic arc, responsible for the geometry and kinematics of second-order structures such as tension cracks, shear factures and volcanic fissures. As is the case of Los Nevados complex, it corresponds to a set of pyroclastic cones and associated lavas located on the northeastern flank of the Villarrica Volcano (Moreno and Clavero, 2006).

2.3. Hot springs

In the study area, there is a significant number of thermal sources of intermediate temperature (Sánchez et al., 2013; Held et al., 2018), which are topographically located in valleys and mostly linked to faults. The thermal sources located along W-NW oriented ATF features, generally present higher reservoir, but lower outflow temperatures, whereas the LOFS favors fast migration of magma and/or hydrothermal fluids (Pérez-Flores et al., 2016; Held et al., 2018). Thus, the thermal waters under the structural control of LOFS are observed to rise with little temperature difference between reservoir and the source as well as low dilution.

3. Magnetotelluric methods

Magnetotelluric is a geophysical exploration technique belonging to the electromagnetic field allowing obtaining information on the geoelectrical properties of the subsurface by the temporal dependent fluctuations of the natural electric (E) and magnetic (H) fields. This technique has been extensively applied in studies of fault zones, volcanic and geothermal systems (Unsworth et al., 1999; Hill et al., 2009; Bertrand et al., 2012; Cordell et al., 2019).

31 magnetotelluric stations have been measured between November and December 2013. The stations have been deployed along two profiles in E–W and N–S direction with a mean inter-station distance of about 3 km between Caburgua Lake and Villarrica Volcano (Fig. 1b). Based on the quality of processing of these data, in this study, the entire dataset was processed using a robust code based on Egbert and Booker (1986) including the 50 Hz filter. Remote referencing leads to significant improvement of transfer function quality in the low frequency range. More information of acquisition, processing and 2-D inversion of the magnetotelluric data are detailed in Held et al. (2016).

Held et al., 2016 evaluated dimensionality by phase sensitive skew of impedance tensor after Bahr, (1991). Results validate the assumption of 2D distribution; however, there are period gaps with high skew (Held et al., 2016, Fig. 4). In this area, the assumption would give unreliable results, particularly in sub-surface near to fault systems and/or hot springs manifestation.

In the presence of heterogeneities considered at the surface, the amplitude of the electric field seen can be distorted. The defined phase tensor seeks to recover the regional phase relationship of a set of distorted measurements, both for surface heterogeneity and for regional conductivity structures are 3D (Caldwell et al., 2004). The phase tensor can be graphically represented by an ellipse with its main axes (Φmax and Φmin). Detailed explanation and analysis of the phase tensor is included in supplementary material. The main resistance structures can identify before modeling by means of phase tensor ellipses, as seen in Fig. 2 with a pseudo section and greater geological features. In the uppermost section, short periods, the ellipses show high scattering in terms of elongation, orientation and mostly high β-angles point to 3-D structures. The change in direction of the principal axes of the phase tensor it is an indicator of a 3-D (regional) conductivity structure. Over long periods, the phase tensor ellipses are affected mainly E–W change in the depth resistivity distribution.

4. 3-D inversion

The 3-D inversion of the magnetotelluric data was carried out using the "Modular System for Inversion of Electromagnetic Geophysical Data, ModEM" developed by Kelbert et al. (2014). It includes forward

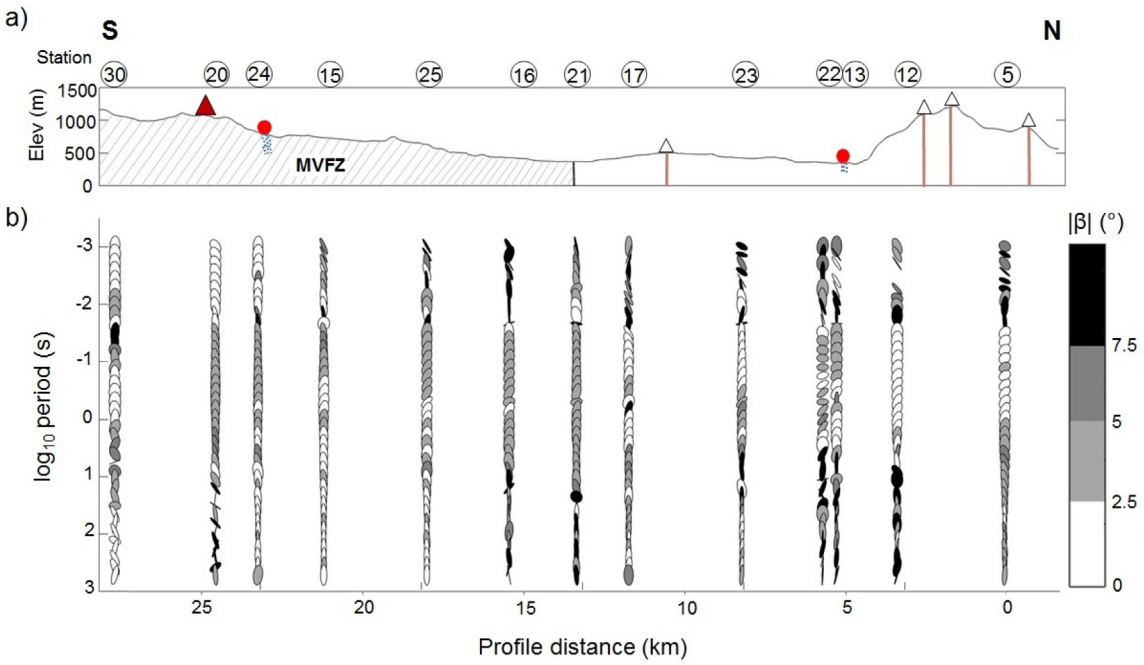

Fig. 2. a) Elevation and major geological features including MVFZ, the monogenetic cones and thermal springs across the N–S profile (Fig. 1). b) Phase tensor ellipse with angle β.

modeling, sensitivity computations, inversion search algorithms, model parametrization and regularization, and data functionals (Kelbert et al., 2014; Egbert and Kelbert, 2012). Its main advantage here is the fast convergence that finally allows for joint inversion of the impedance tensor together with the induction vector.

A subset of the data has been chosen to efficiently use the 3-D inversion program, calculated in 43 periods, logarithmically distributed between 0.0026 s and 512 s, with 7 periods per decade. All the elements of impedance tensor Z and vertical magnetic component are relevant. In this study, we established a data error of 10% of $|ZxyZyx|^{1/2}$ and 10% of $|TyTx|^{1/2}$, starting from a homogeneous half-space of 100 Ωm. The level of error was determined by the low data quality stations due to the presence of noise. A regular grid centered at the crossing of the E–W and N–S profiles was defined. The grid extends over 70 (E–W, positive towards the east) × 90 (N–S, positive towards the north) cells with a uniform size of 500 m × 500 m with 10 padding cells in each direction increasing gradually. To avoid lateral boundary effects, these padding cells with increasing size of the factor 1.3 were added. Topography was included using 50 m cells of linear increase up to 2000 m to continue with an increase factor of 1.1, allowing including topographic relief in whole region with a maximum elevation of 2847 m a.s.l. and minimum elevation of 243 m a.s.l. The increasing size in vertical direction sums up 89 layers. In total, the grid represents a volume of 70 km × 90 km × 89 km.

3-D inversion started from a homogeneous half-space of 100 Ωm. The best-fit model was achieved after 82 iterations with a normalized

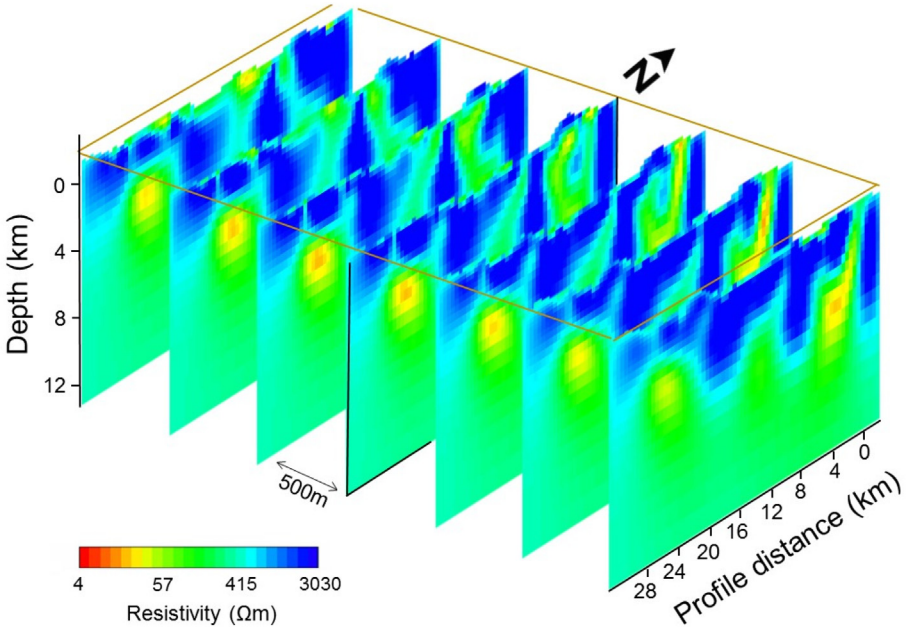

Fig. 3. N–S cross-sections of the 3-D inversion of magnetotelluric data across the LOFS with an offset of 500 m to each other and including the majority of the measured MT stations (sections I–VII in Fig. 1c).

RMS error of 2.18. For examples of the data fit, see Fig. S3 in the supporting information. The inversion results along the LOFS are presented in seven N–S profiles parallel to the LOFS (from its eastern branch in the north to the presumed outline through the MVFZ) with distances of 500 m to each other in Fig. 3. The resistivity distribution along the LOFS is highly variable down to approximately 8 km depth. The near-surface is characterized by a resistivity ranging from a few Ωm to a few thousands Ωm that are distributed very locally. Below, a background resistivity of a few thousands Ωm extends down to about 4–5 km depth. This background is interrupted locally by low resistivity in the few Ωm to few tens or few hundreds Ωm range. In the northern part, some of these anomalies root rather deep. On the other hand, the prominent low resistivity anomaly in the south seems more root shallow. It reveals a resistivity minimum in the central profiles, whereas the northern low resistivity anomaly is most prominent in the eastern profiles. Below about 8 km, a resistivity of a 100 Ωm is prevalent. Comparable changes in electric resistivity have been attributed to the brittle-ductile transition zone (Bertrand et al., 2012) or changes in magnetic properties at the boundary between the upper and middle crust (Hernandez-Moreno et al., 2014).

5. Discussion

5.1. Influence of the main structures on dimensionality

Results of the 3D model of resistivity distribution for the subsurface are consistent with main resistance features predicted before modeling by phase tensor analysis. As observed, high values of β angle, high dispersion in Φmax orientation and elongated ellipses indicate three-dimensional effects in short periods. In the inversion model, the 3D effects are observable up to 0.25 km a.s.l. (Fig. 4a). The 3D effects would be ascribed to different Holocene volcanic stratigraphic layers belonging to several eruptive episodes of the Villarrica-Quetrupillan-Lanin volcanic chain.

At 0.4 km b.l.s. (Fig. 4b) structures begin to be identified on a larger scale. MT sites deployed parallel to LOFS exhibit a trend of both low electrical resistivity and high electrical resistivity anomalies accommodated following the LOFS NS alignment, evidencing the presence of LOFS throughout the study area (Fig. 1b). In turn, the difference in the electrical response would be related to the degree of damage to the fault. Greater fracturing favors the infiltration of hydrothermal fluids, decreasing the resistivity in the rocks. Implications of physical properties are discussed in next sections.

Enhanced of electrical response are mainly noticeable in the northern part of LOFS (Fig. 4c), where the monogenetic cones are located. According to the spatial distribution and organization of individual volcanic buildings and cluster of volcanoes, the volcanic-tectonic association of LOFS would be evident.

From 2 km depth to 4 km, both fault systems would play a leading role. The lowest resistivity anomalies are related to N–S tectonic structures (LOFS) and partly NW–SE (MVFZ). We interpret this interaction as a favorable place for the development of highly fractured areas, facilitating the appearance of horizontal conductive anomalies. Below 4 km (Fig. 4d), low resistivity anomalies would be highly influenced by active/inactive basement faults (ATFs).

5.2. 2- versus 3-D inversion results

For comparison with 2-D inversion (Held et al., 2016) and volcanic and geothermal manifestations, two representative cross-sections of the 3-D inversion results are presented in Figs. 5 and 6.

Since the main geo-electric strike is parallel to the LOFS, the comparison between 2-D and 3-D inversion is provided for the E–W section (Fig. 5). The resistivity distribution obtained from 2-D inversion reveals a resistive environment down to about 7.5 km depth crosscut by an intermediate conductive anomaly at the LOFS (Fig. 5a; Held et al., 2016). In the 3-D inversion, resistivity of this zone reaches lower values and its vertical extension to about 5 km is smaller. Its lateral resistivity variation reveals a higher dynamic. In contrast, to geological indications pointing to an about 2 km broad LOFS between the two boundary faults along each side of Caburgua Lake, the 2-D forward modeling of magnetotelluric data revealed a lateral extension of the LOFS about 0.25 km fixed to the eastern branch of the LOFS as best fit to the intermediate anomaly. The high-resolution image obtained in this study by 3-D inversion confirms this picture, but reveals a rather narrow branch rooting in the deep anomaly C_1 at this eastern branch of LOFS (Fig. 5b).

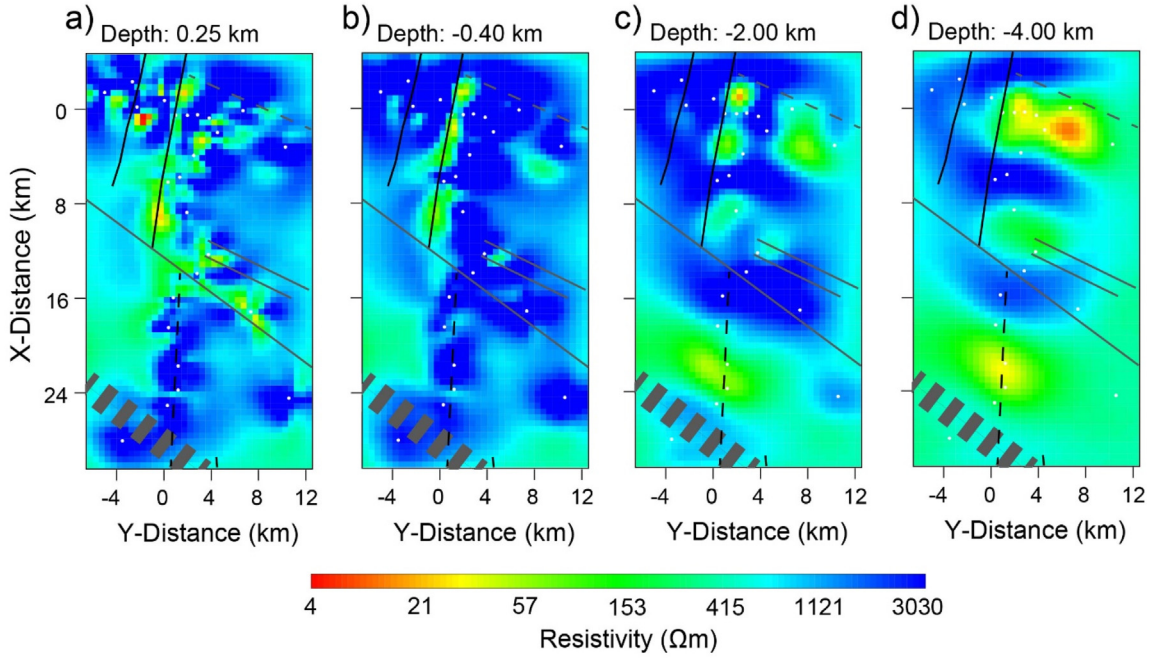

Fig. 4. Plan view 3D Model results focused on the area with the highest density of stations shown 4 horizontal slices through the model at approximate depths of a) 0.25 km a.s.l., b) 0.40 km b.l.s., c) 2.00 km b.l.s., and d) 4.00 km b.l.s. Location of the MT stations are represented by white dots. Major fault traces of LOFS and ATFs are represented by black and gray lines, respectively.

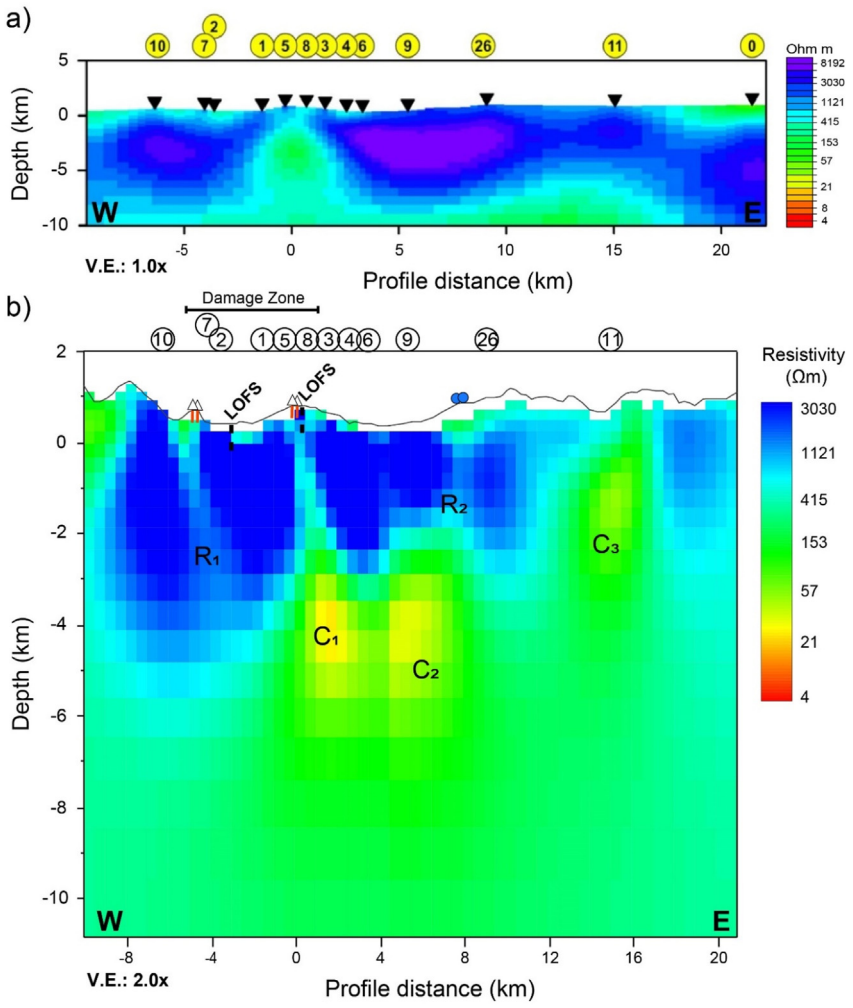

Fig. 5. E–W section of a) the 2-D inverted electric resistivity distribution along east-west profile modified from Held et al. (2016), and b) the 3-D inverted electric resistivity distribution of section VIII in Fig. 1. High and intermediated conductivity anomalies are labeled with $C_1/C_2/C_3$ and R_1/R_2, respectively. Anomaly C_1 corresponds to the C_1 in Fig. 6. Elevation (gray line) and major geological features including MVFZ, the monogenetic cones and thermal springs across the N–S profile (Fig. 1) are included. In the top of each graph, MT stations (circles) of the profiles are shown.

In the section that is well-covered by magnetotelluric stations (between −8 and 8 km in Fig. 5), our high resolution results reveal a number of low-resistivity anomalies (about <20 Ωm, C_1 and C_2) as well as one of intermediate values (several hundreds of Ωm, $R_1$and R_2). While the anomaly R_1 is roughly indicated and the anomaly C_2 occurs at deeper levels in the 2-D inversion. The anomaly C_3 is revealed by 3-D inversion, only. Due to the limited number of stations in this area, one must be careful in interpreting these anomalies. However, it would also occur at deeper levels in the 2-D inversion Anomaly C3 would represent an overestimated anomaly of less resistivity than surrounding area located at shallow depth between stations 11 and 0 in Held et al., 2016 (Fig. 5a).

5.2.1. Why are important characteristics not evident in long periods in 3D inversion?

Discussed in the previous section, both the vertical extension of the resistivity distribution is less compared to 2D inversion and the C2 anomaly occurs at shallower levels. Sensitivity tests have been performed to verify the reliability of these features, adjusting different setup focused in main anomalies located below 3 km.

As shown in the supplementary material, replacing anomalies poor fit for intermediate and long periods obtained compared to the selected model. In the case of intermediate periods, the worst fit is directly related to the location of the modified features. For long periods, inversions are struggling to adjust some important features in absence of conductive anomalies (for example, Con2 in Held et al., 2016). Most distinguishable problem is in sites near to this feature. This behavior in 2D inversion has also been observed. To solve this issue in 2D inversion, the preferred model was obtained with error floor 70% for TE mode, which is predominant to detect conductive features. In our case, as the goal is on the features at medium to shallow depths, we set 10% error floor for both modes.

5.3. High-resolution resistivity distribution along the LOFS

Fig. 6 displays the resistivity anomalies obtained from 3-D inversion along the section IV in Figs. 1 and 3 that is subparallel to the LOFS covering from north to south its eastern branch, several monogenetic cones, two thermal springs and reaching the MVFZ towards the El Mocho volcano. In contrast to section VII, the magnetotelluric station coverage and data quality along the profile is rather homogenous. Thus, resistivity anomalies along the section are equally reliable.

A low-resistivity anomaly extends from the surface to about 7 km depth in the northern part of the profile (C_1), revealing two branches towards the surface, a southern and a northern branch. While along section IV the northern branch appears to be dominant, towards the east in the sections VI and VII, the southern branch develops to the surface and reveals increasing electric conductivity (Fig. 3). Highest electric conductivity in this section occurs in the southern part of the section

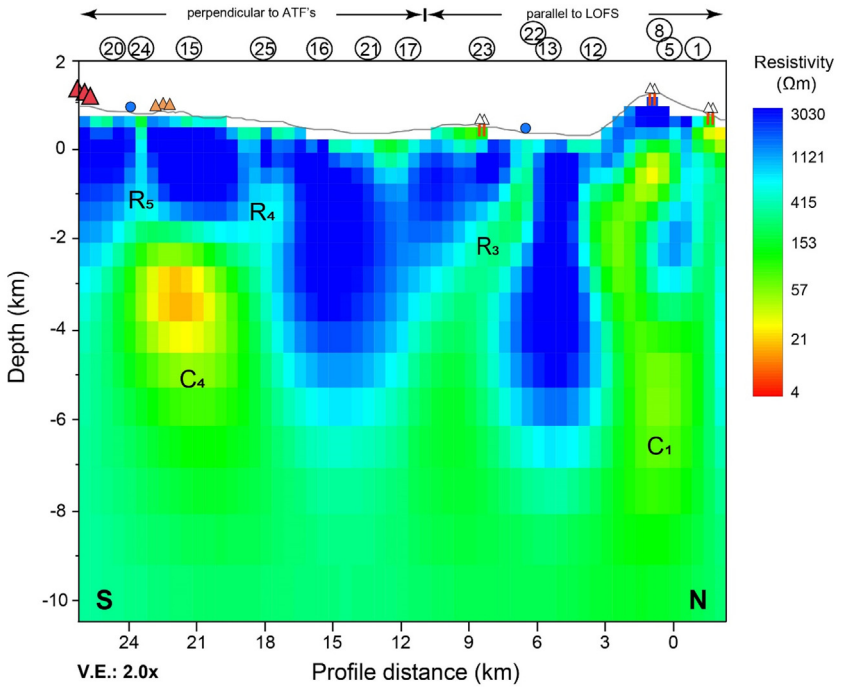

Fig. 6. N–S section subparallel to the LOFS in the study area of the 3-D inverted electrical resistivity distribution of section IV in Figs. 1 and 4. This profile corresponds to the central profile in Fig. 3. High and intermediated conductivity anomalies are labeled with C_1/C_4 and $R_3/R_4/R_5$, respectively. Anomaly C_1 corresponds to the C_1 in Fig. 5. Elevation (gray line) and major geological features, the monogenetic cones and thermal springs across the N–S profile (Fig. 1).

towards the volcanic chain at a depth of about 3–4 km. Although intermediate resistivity values are observed throughout the entire model above this anomaly C_4, it appears to be rather connected from the surface (Los Nevados complex). Major intermediate resistivity anomalies crosscutting the resistive body down to about 4 km depth, R_4 and R_5, occur at the edges of C_4, while R_3, the anomaly with the highest conductivity seems to represent a more important structure.

5.4. Comparison between geothermal and magmatic manifestations and resistivity

A summary of the observed anomalies in the representative cross sections (Figs. 5b and 6) and their connection to volcanic and geothermal manifestations at the surface is provided in Table 1. It results that low-resistivity anomalies are typically occurring at depth > 4 km. The anomaly C_1 coincides with the eastern branch of the LOFS and connects to the surface, where it reveals resistivity of a few hundreds of Ωm. Along its extension of about 5 km to the north, a number of monogenetic cones are observed at the surface. It should be mentioned that south of anomaly C_1, the representative profile deviates from the mapped surface outline of the LOFS.

Anomalies of intermediate resistivity are typically limited to depths <1 or <2 km. The anomaly R_2 is an exception and links to a fault zone that is part of the ATFs and hosts thermal springs that reveal reservoir temperature that are among the highest in the area (120–140 °C; Held et al., 2018). The anomalies R_3 and R_5 are linked to thermal springs of reservoir temperatures of about 100–110 °C. The deeper-rooting intermediate resistivity anomalies R_1 and R_4 are not connected to a thermal springs. R_1 links monogenetic cones at the western branch of Caburgua Lake, the so-called Caburgua cluster with an age of about 8000–6000 yrs. (Moreno and Clavero, 2006). Although a clear anomaly appears, no manifestations are observed at the surface linked to R_4. This anomaly develops into a near surface low-resistivity anomaly towards the west, where the easternmost volcanic cones of the Villarrica Volcano occur. Interestingly, this coincides with the change in orientation of the phase tensors from approximately N–S to about N30–40°E at the stations 25 and 16 and about N60°E further to the north at periods of about 1 s.

The origin of C_2 and C_4 is largely unknown. Kapinos et al. (2016) have suggested that this type of anomalies represent magma chambers.

5.5. Implications of the physical properties

5.5.1. Porosity effects in resistivity response in faults

The effects of porosity in shear fault zones in the upper crust have been estimated using magnetotelluric in different parts of the world (Unsworth et al., 1999; Bredosian et al., 2004; Becken et al., 2008; Yoshimura et al., 2009). Fault systems generate anomalies of lower resistivity than their environment, by fractures, increasing porosity and infiltrating hydrothermal fluids with salt content, improving the electrical properties of the rocks.

Table 1
Summary of the range of extension in depth of the observed low (C) and intermediate (R) resistivity anomalies and the connected volcanic and geothermal manifestations at the surface from Figs. 5 and 6.

Depth extension (km)	0 to 2	0 to >5	>2 to >5
Anomalies (connected surface manifestations)	R_1 (monogenetic cones, LOFS-western branch) R_2 (Thermal springs) R_4 (volcanic cones/MVFZ?) R_5 (thermal spring)	R_3 (thermal spring, monogenetic cone?) C_1 (LOFS-eastern branch, monogenetic cones)	C_2 (−) C_4 (Los Nevados complex?)

While Held et al., 2016 provide properties insights of LOFS, significant assumptions are required for fault zone parameters such as cementing factor, porosity, and clay content that are currently not well defined. Resistivity depends on the properties of the host rock and the content of fluids, since the dependence of the geoelectric response of the rocks on the crust is controlled by the ions contained in the water enclosed in pores. Therefore, the electrical response in rocks varies proportionally to the increase in porosity, temperature or molten fraction.

The role of the fluid in resistivity is determined by the amount of electrolytes that interconnect through the pores of the rock. Thus, a high percentage of porosity filled with saline fluids decreases the resistivity. Taking into account the characteristics of geothermal fluids in the Villarrica area (Nitschke et al., 2016); Saline fluid resistivity estimated at ~10 Ωm and cementing factor between 1 and 1.3, quantifications for the C_1 anomaly on the LOFS by Archie's law (Archie, 1942) reveal a required porosity range of 5–20%. This range is coherent with porosity values in shear fault zone, therefore the partial fraction option has been excluded for this characteristic, being consistent with the hypothesis that magmas would have migrated directly to the surface through LOFS from the deep reservoir (Morgado et al., 2015). Then, anomaly C_1 would represent the place where fluids accumulate in a large, damaged, high-porosity area produced by rock fracture at ~4 km depth, from where fluid flows to the surface along the interface acting as a preferential medium temperature fluid exchange route. Furthermore, the location of the C_1 anomaly (Fig. 6) below the Caburgua monogenetic cones, would confirm the hypothesis that the eastern branch of LOFS facilitated the rise of magma and reveals a vertical pathway extending to the surface.

R_1 anomaly, located below the group of monogenetic cones and in western branch, LOFS would also have functioned as a direct ascending conduit for magma. Here, we assume the same hydrothermal fluid fills the fractures, since it is part of the damage zone. Quantifications for the R1 anomaly reveal a porosity of <5%. Therefore, we infer that the western branch of LOFS is a more cohesive area with less content of hydrothermal fluids.

5.5.2. Implication of melt fraction in high conductivity features

Explaining high conductivity in anomaly C_4 presents greater complexity than the case previously analyzed for C_1. The absence of a main branch of LOFS makes the porosity analysis based on fracture parameters of this fault difficult. On the other hand, the presence of the group of young volcanic buildings, Los Nevados, suggests the presence of a certain amount of melt fraction, validated by the hypothesis of a shallow intermediate deposit for elaborate magmas belonging to the Villarrica volcanic chain (Morgado et al., 2015).

Taking into account the pyroclastic cones that compose Los Nevados group are oriented N60°E, this alignment would reflect fissures through magmas would have reached the surface (Moreno and Clavero, 2006), we can estimate the porosity by Archie's law. Applying same assumptions for C_1, hydrothermal fluids and cementing factor range reveal a required porosity range of 20–60%. Range considered unreliable, due to geological considerations, therefore, the surrounding area of this anomaly would be discarded as a direct ascent pathways.

In order to characterize this high conductivity structures, their possible origin was estimated incorporating the melt fraction based on Archie's modified law (Glover et al., 2000). Taking into account melt fraction between 2 and 10% with a conductivity of 10 S m^{-1} based on the range of electrical conductivity of the andesitic molten rock stablished by Tyburczy and Waff (1983), and the best porosity range scenario of 10–20% with cementation factor m = 1.3–1.6, we can explain a resistivity bulk of 15–20 Ωm. Therefore, the resistivity values obtained for the model with the best data fit, this conductive anomaly could be related to a remaining conduit or shallow reservoir of andesitic-basaltic composition.

5.6. Volcanic seismic background

Mora Stock (2015) detects a low seismic velocity zone located east of the main building of the Villarrica Volcano, where the group of volcanic cones of Los Nevados complex are located. This zone of low velocity matches in location and depth with the structure of low resistive anomaly (C_4) coincides with the second-order structures such as tension cracks, shear factures and volcanic fissures described by Cembrano and Lara, 2009 Fig. 6F. As we discussed in previous section, the feature C_4 would be interpreted as a remnant conduit/dike. Sensitivity data of C_4 has been evaluated by sensitivity test (Fig. S4 in the support material) to delimit the possible magnitudes of this feature.

6. Conclusions

In this study, we demonstrate the potential of 3-D inversion of a magnetotelluric station network for detecting preferential fluid pathway along fault zones. Compared to earlier 2-D inversion, here, all anomalies of intermediate depth that are mostly of intermediate conductivity are traced up to the surface, where seven out of eight can be clearly linked to volcanic or geothermal surface manifestations. Phase tensor analyses indicate a structural origin of the high conductivity anomaly that may be connected to a line of volcanic cones that occurs in the NE of the Villarrica Volcano.

Deep and highly conductive anomalies are detected in the vicinity of the volcanic chain and the crossing of major faults, in our case LOFS and a fault that belongs to the ATF system. The connection to the surface is very clear for the fault-related system, where crossing of two damage zones may provide optimal vertical pathways. The link between the volcanic chain and the deep anomaly in the south of the study zone is less evident. For further clarification, an extension of the high-resolution data set towards the Villarrica Volcano would be necessary.

Our results have major implications for the understanding of the subsurface of the Villarrica Volcano, of which little is known. More important, the results of the 3-D inversion of high-resolution magnetotelluric data reveal great potential for geothermal exploration. The link between electric conductivity and thermal springs reveals images and depth of the respective hydrothermal reservoir.

Declaration of competing interests

The authors declare that they have no known competing financial interests or personal relationships that could have appeared to influence the work reported in this paper.

CRediT authorship contribution statement

Maximiliano Pavez: Conceptualization, Methodology, Formal analysis, Software, Investigation, Validation, Writing - original draft, Writing - review & editing, Project administration, Funding acquisition.**Eva Schill:**Conceptualization, Methodology, Investigation, Writing - original draft, Writing - review & editing, Supervision. **Sebastian Held:**Conceptualization, Investigation, Writing - review & editing, Formal analysis.**Daniel Díaz:**Investigation, Writing - review & editing, Software.**Thomas Kohl:**Writing - review & editing, Funding acquisition, Supervision.

Acknowledgements

The study is part of a collaborative research project between Karlsruhe Institute of Technology (KIT) and the Andean Geothermal Center of Excellence (CEGA, FONDAP-CONICYT 15090013).

The authors appreciate the support from the BMBF-CONICYT International Scientific Collaborative Research Program (FKZ 01DN14033/PCCI130025). M. Pavez appreciates the support by the National Agency

for Research and Development (ANID)/Scholarship Program/DOCTORADO BECAS CHILE-DAAD/2015 – 62150016. We thank Gary Egbert and Anna Kelbert for the use of their ModEM inversion program and special thanks to Naser Meqbel for providing visualization program. BwUniCluster computer clusters were used for 3-D inversion.

Appendix A. Supplementary data

Supplementary data to this article can be found online at https://doi.org/10.1016/j.jvolgeores.2020.106913.

References

Archie, G.E., 1942. The electrical resistivity log as an aid in determining some reservoir characteristics. Trans. AIME 146 (1), 54–62.

Bahr, K., 1991. Geological noise in magnetotelluric data: a classification of distortion types. Physics of the Earth and Planetary Interiors 66 (1–2), 24–38.

Barton, C.A., Zoback, M.D., Moos, D., 1995. Fluid flow along potentially active faults in crystalline rock. Geology 23 (8), 683–686.

Becken, M., Ritter, O., Bredosian, P.A., Weckmann, U., Weber, M., 2008. A deep crustal fluid channel into the San Andreas Fault system near Parkfield, California. Geophysical Journal International 173 (2), 718–732.

Bense, V.F., Gleeson, T., Loveless, S.E., Bour, O., Scibek, J., 2013. Fault zone hydrogeology. Earth Sci. Rev. 127, 171–192.

Bertrand, E.A., Caldwell, T.G., Hill, G.J., Wallin, E.L., Bennie, S.L., Cozens, N., Onacha, S.A., Ryan, G.A., Walter, C., Zaino, A., Wameyo, P., 2012. Magnetotelluric imaging of upper-crustal convection plumes beneath the Taupo Volcanic Zone, New Zealand. Geophys. Res. Lett. 39 (2).

Brasse, H., Soyer, W., 2001. A magnetotelluric study in the Southern Chilean Andes. Geophys. Res. Lett. 28 (19), 3757–3760.

Bredosian, P.A., Unsworth, M.J., Egbert, G.D., Thurberd, C.H., 2004. Geophysical images of the creeping segment of the San Andreas fault: implications for the role of crustal fluids in the earthquake process. Tectonophysics 385 (1–4), 137–158. https://doi.org/10.1016/j.tecto.2004.02.010.

Brown, S., Bruhn, R., 1998. Fluid permeability of deformable fracture networks. J. Geophys. Res. 103 (B2), 2489–2500.

Caldwell, T.G., Bibby, H.M., Brown, C., 2004. The magnetotelluric phase tensor. Geophys. J. Int. 158 (2), 457–469.

Cembrano, J., Lara, L., 2009. The link between volcanism and tectonics in the southern volcanic zone of the Chilean Andes: a review. Tectonophysics 471 (1–2), 96–113.

Cembrano, J., Hervé, F., Lavenu, A., 1996. The Liquiñe Ofqui fault zone: a long-lived intra-arc fault system in southern Chile. Tectonophysics 259 (1–3), 55–66.

Cembrano, J., Schermer, E., Lavenu, A., Sanhueza, A., 2000. Contrasting nature of deformation along an intra-arc shear zone, the Liquiñe–Ofqui fault zone, southern Chilean Andes. Tectonophysics 319 (2), 129–149.

Cembrano, J., Lavenu, A., Reynolds, P., Arancibia, G., López, G., Sanhueza, A., 2002. Late Cenozoic transpressional ductile deformation north of the Nazca–South America–Antarctica triple junction. Tectonophysics 354 (3–4), 289–314.

Cordell, D., Unsworth, M.J., Diaz, D., Reyes-Wagner, V., Currie, C.A., Hicks, S.P., 2019. Fluid and melt pathways in the Central Chilean subduction zone near the 2010 Maule earthquake (35–36° S) as inferred from magnetotelluric data. Geochem. Geophys. Geosyst. 20, 1818–1835. https://doi.org/10.1029/2018GC008167.

Díaz, D., Heise, W., Zamudio, F., 2015. Three-dimensional resistivity image of the magmatic system beneath Lastarria Volcano and evidence for magmatic intrusion in the back arc (northern Chile). Geophys. Res. Lett. 42 (13), 5212–5218.

Egbert, G.D., Booker, J.R., 1986. Robust estimation of geomagnetic transfer functions. Geophys. J. R. Astron. Soc. 87 (1), 173–194.

Egbert, G.D., Kelbert, A., 2012. Computational recipes for electromagnetic inverse problems. Geophys. J. Int. 189 (1), 251–267.

Geiermann, J., Schill, E., 2010. 2-D magnetotellurics at the geothermal site at Soultz-sous-Forêts: resistivity distribution to about 3000 m depth. Compt. Rendus Geosci. 342 (7–8), 587–599.

Glover, P.W.J., Hole, M.J., Pous, J., 2000. A modified Archie's law for two conducting phases. Earth Planet. Sci. Lett. 180, 369–383.

Heise, W., Caldwell, T.G., Bibby, H.M., Bannister, S.C., 2008. Three-dimensional modelling of magnetotelluric data from the Rotokawa geothermal field, Taupo Volcanic Zone, New Zealand. Geophys. J. Int. 173 (2), 740–750.

Held, S., Schill, E., Pavez, M., Díaz, D., Muñoz, G., Morata, D., Kohl, T., 2016. Resistivity distribution from mid-crustal conductor to near-surface across the 1200 km long Liquiñe-Ofqui Fault System, southern Chile. Geophys. J. Int. 207 (3), 1387–1400.

Held, S., Schill, E., Schneider, J., Nitschke, F., Morata, D., Neumann, T., Kohl, T., 2018. Geochemical characterization of the geothermal system at Villarrica Volcano, southern Chile; part 1: impacts of lithology on the geothermal reservoir. Geothermics 74, 226–239.

Hernandez-Moreno, C., Speranza, F., Di Chiara, A., 2014. Understanding kinematics of intra-arc transcurrent deformation: paleomagnetic evidence from the Liquiñe-Ofqui fault zone (Chile, 38–41° S). Tectonics 33 (10), 1964–1988.

Hickey-Vargas, R., Roa, H.M., Escobar, L.L., Frey, F.A., 1989. Geochemical variations in Andean basaltic and silicic lavas from the Villarrica-Lanin volcanic chain (39.5 S): an evaluation of source heterogeneity, fractional crystallization and crustal assimilation. Contrib. Mineral. Petrol. 103 (3), 361–386.

Hickey-Vargas, R., Sun, M., Holbik, S., 2016. Geochemistry of basalts from small eruptive centers near Villarrica stratovolcano, Chile: evidence for lithospheric mantle components in continental arc magmas. Geochim. Cosmochim. Acta 185, 358–382.

Hill, G.J., Caldwell, T.G., Heise, W., Chertkoff, D.G., Bibby, H.M., Burgess, M.K., Cull, J.P., Cas, R.A., 2009. Distribution of melt beneath Mount St Helens and Mount Adams inferred from magnetotelluric data. Nat. Geosci. 2 (11), 785.

Jones, G.A., Groom, R.W., 1993. Strike-angle determination from the magnetotelluric impedance tensor in the presence of noise and local distortion: rotate at your peril! Geophysical Journal International 113 (2), 524–534. https://doi.org/10.1111/j.1365-246X.1993.tb00905.x.

Kapinos, G., Montahaei, M., Meqbel, N., Brasse, H., 2016. Three-dimensional electrical resistivity image of the South-Central Chilean subduction zone. Tectonophysics 666, 76–89.

Kelbert, A., Meqbel, N., Egbert, G.D., Tandon, K., 2014. ModEM: a modular system for inversion of electromagnetic geophysical data. Comput. Geosci. 66, 40–53.

Lange, D., Cembrano, J., Rietbrock, A., Haberland, C., Dahm, T., Bataille, K., 2008. First seismic record for intra-arc strike-slip tectonics along the Liquiñe-Ofqui fault zone at the obliquely convergent plate margin of the southern Andes. Tectonophysics 455 (1–4), 14–24.

Lara, L., 2004. Villarrica-Lanin chain: tectonic constraints for volcanism in a transversal alignment. Villarrica Volcano (39.5 S), Southern Andes, Chile (Lara, L), pp. 13–16.

Lara, L.E., Moreno, H., 2004. Mapa geología del área Liquiñe-Neltume. Carta Geológica de Chile, Serie Geología Básica, p. 83.

Lara, L.E., Naranjo, J.A., Moreno, H., 2004. Lanín volcano (39.5° S), Southern Andes: geology and morphostructural evolution. Rev. Geol. Chile 31 (2), 241–257.

Lara, L.E., Lavenu, A., Cembrano, J., Rodríguez, C., 2006a. Structural controls of volcanism in transversal chains: resheared faults and neotectonics in the Cordón Caulle–Puyehue area (40.5 S), Southern Andes. J. Volcanol. Geotherm. Res. 158 (1–2), 70–86.

Lara, L.E., Moreno, H., Naranjo, J.A., Matthews, S., de Arce, C.P., 2006b. Magmatic evolution of the Puyehue–Cordón Caulle Volcanic Complex (40 S), Southern Andean Volcanic Zone: from shield to unusual rhyolitic fissure volcanism. J. Volcanol. Geotherm. Res. 157 (4), 343–366.

Lavenu, A., Cembrano, J., 1999. Compressional-and transpressional-stress pattern for Pliocene and Quaternary brittle deformation in fore arc and intra-arc zones (Andes of Central and Southern Chile). J. Struct. Geol. 21 (12), 1669–1691.

López-Escobar, L., Cembrano, J., Moreno, H., 1995. Geochemistry and tectonics of the Chilean Southern Andes basaltic Quaternary volcanism (37–46 S). Andean Geol. 22 (2), 219–234.

McGee, L.E., Brahm, R., Rowe, M.C., Handley, H.K., Morgado, E., Lara, L.E., Turner, M.B., Vinet, N., Parada, M.A., Valdivia, P., 2017. A geochemical approach to distinguishing competing tectono-magmatic processes preserved in small eruptive centres. Contrib. Mineral. Petrol. 172 (6), 44.

Melnick, D., Folguera, A., Ramos, V.A., 2006. Structural control on arc volcanism: the Caviahue–Copahue complex, Central to Patagonian Andes transition (38 S). J. S. Am. Earth Sci. 22 (1–2), 66–88.

Mora Stock, C.N., 2015. Seismic Structure and Seismicity of the Villarrica Volcano (Southern Central Chile). Doctoral dissertation. Christian-Albrechts-Universität.

Moreno, H., Clavero, J., 2006. Geología del volcán Villarrica, Regiones de la Araucanía y de los Lagos. Servicio Nacional de Geología y Minería. Carta Geológica de Chile, Serie Geología Básica 98 (1).

Morgado, E., Parada, M.A., Contreras, C., Castruccio, A., Gutiérrez, F., McGee, L.E., 2015. Contrasting records from mantle to surface of Holocene lavas of two nearby arc volcanic complexes: Caburgua-Huelemolle small eruptive centers and Villarrica Volcano, Southern Chile. J. Volcanol. Geotherm. Res. 306, 1–16.

Nitschke, F., Held, S., Villalon, I., Mundhenk, N., Kohl, T., Neumann, T., 2016. Geochemical reservoir exploration and temperature determination at the Mt. Villarrica geothermal system, Chile. Proceeding European Geothermal Congress, pp. 19–24.

Pérez-Flores, P., Cembrano, J., Sánchez-Alfaro, P., Veloso, E., Arancibia, G., Roquer, T., 2016. Tectonics, magmatism and paleo-fluid distribution in a strike-slip setting: insights from the northern termination of the Liquiñe–Ofqui fault System, Chile. Tectonophysics 680, 192–210.

Pinel, V., Jaupart, C., 2000. The effect of edifice load on magma ascent beneath a volcano. Philos. Trans. R. Soc. A Math. Phys. Eng. Sci. 358 (1770), 1515–1532.

Rosenau, M., Melnick, D., Echtler, H., 2006. Kinematic constraints on intra-arc shear and strain partitioning in the southern Andes between 38° S and 42° S latitude. Tectonics 25 (4).

Sánchez, P., Pérez-Flores, P., Arancibia, G., Cembrano, J., Reich, M., 2013. Crustal deformation effects on the chemical evolution of geothermal systems: the intra-arc Liquiñe–Ofqui fault system, Southern Andes. Int. Geol. Rev. 55 (11), 1384–1400.

http://portalgeomin.sernageomin.cl:6080/arcgis/rest/services/geoportal/GeologiaBase/MapServer/3.

Somoza, R., 1998. Updated Azca (Farallon)—South America relative motions during the last 40 My: implications for mountain building in the central Andean region. J. S. Am. Earth Sci. 11 (3), 211–215.

Tyburczy, J.A., Waff, H.S., 1983. Electrical conductivity of molten basalt and andesite to 25 kilobars pressure: geophysical significance and implications for charge transport and melt structure. J. Geophys. Res. 88 (B3), 2413–2430.

Unsworth, M., Bedrosian, P.A., 2004a. On the geoelectric structure of major strike-slip faults and shear zones. Earth Planets Space 56 (12), 1177–1184.

Unsworth, M., Bedrosian, P.A., 2004b. Electrical resistivity structure at the SAFOD site from magnetotelluric exploration. Geophys. Res. Lett. 31, L12S05. https://doi.org/10.1029/2003GL019405.

Unsworth, M., Egbert, G., Booker, J., 1999. High-resolution electromagnetic imaging of the San Andreas Fault in Central California. J. Geophys. Res. Solid Earth 104 (B1), 1131–1150.

Walker, R.J., Holdsworth, R.E., Armitage, P.J., Faulkner, D.R., 2013. Fault zone permeability structure evolution in basalts. Geology 41 (1), 59–62. https://doi.org/10.1130/G33508.1.

Wrage, J., Tardani, D., Reich, M., Daniele, L., Arancibia, G., Cembrano, J., Sanchez-Alfaro, P., Morata, D., Pérez-Moreno, R., 2017. Geochemistry of thermal waters in the Southern Volcanic Zone, Chile—implications for structural controls on geothermal fluid composition. Chem. Geol. 466, 545–561.

Yoshimura, R., Oshiman, N., Uyeshima, M., Toh, H., Uto, T., Kanezaki, H., et al., 2009. Magnetotelluric transect across the Niigata-Kobe Tectonic Zone, central Japan: A clear correlation between strain accumulation and resistivity structure. Geophys. Res. Lett. 36 (20).